Physics of Fluids

# Wall-modeled large-eddy simulations of spanwise rotating turbulent channels—Comparing a physics-based approach and a data-based approach

Cite as: Phys. Fluids **31**, 125105 (2019); https://doi.org/10.1063/1.5129178
Submitted: 26 September 2019 . Accepted: 14 November 2019 . Published Online: 06 December 2019

Xinyi L. D. Huang (黄馨仪), Xiang I. A. Yang (杨翔), and Robert F. Kunz

Physics of Fluids ARTICLE scitation.org/journal/phf

# Wall-modeled large-eddy simulations of spanwise rotating turbulent channels—Comparing a physics-based approach and a data-based approach

Cite as: Phys. Fluids 31, 125105 (2019); doi: 10.1063/1.5129178
Submitted: 26 September 2019 • Accepted: 14 November 2019 •
Published Online: 6 December 2019

View Online Export Citation CrossMark

Xinyi L. D. Huang (黄馨仪), Xiang I. A. Yang (杨翔),[a] and Robert F. Kunz

## AFFILIATIONS

[1] Department of Mechanical Engineering, Pennsylvania State University, State College, Pennsylvania 16802, USA

[a)] xzy48@psu.edu

## ABSTRACT

We develop wall modeling capabilities for large-eddy simulations (LESs) of channel flow subjected to spanwise rotation. The developed models are used for flows at various Reynolds numbers and rotation numbers, with different grid resolutions and in differently sized computational domains. We compare a physics-based approach and a data-based machine learning approach. When pursuing a data-based approach, we use the available direct numerical simulation data as our training data. We highlight the difference between LES wall modeling, where one writes all flow quantities in a coordinate defined by the wall-normal direction and the near-wall flow direction, and Reynolds-averaged Navier-Stokes modeling, where one writes flow quantities in tensor forms. Pursuing a physics-based approach, we account for system rotation by reformulating the eddy viscosity in the wall model. Employing the reformulated eddy viscosity, the wall model is able to predict the mean flow correctly. Pursuing a data-based approach, we train a fully connected feed-forward neural network (FNN). The FNN is informed about our knowledge (although limited) on the mean flow. We then use the trained FNNs as wall models in wall modeled LES (WMLES) and show that it predicts the mean flow correctly. While it is not the focus of this study, special attention is paid to the problem of log-layer mismatch, which is common in WMLES. Our study shows that log-layer mismatch, or rather, linear-layer mismatch in WMLES of spanwise rotating channels, is not present at high rotation numbers, even when the wall-model/LES matching location is at the first grid point.



## I. INTRODUCTION

Resolving all the energy-containing scales in a high Reynolds number wall-bounded flow simulation is costly.[1,2] A more cost-effective approach is to resolve the relatively large eddies and model the near-wall small-scale (but yet energy-containing) eddies. This leads to wall-modeled large-eddy simulations (WMLESs), in which the effects of the near-wall turbulent eddies are modeled through a large-eddy simulation (LES) wall model. A wall model computes the local wall-shear stress from the resolved flow field in a low-speed flow. The computed wall-shear stress is used as the boundary condition of the LES equations.[3] Figure 1(b) shows the typical setup of a WMLES.

In the past decade or so, this cost-effective tool, WMLES, was used for high Reynolds number flat-plate boundary layers,[4,5] rough-wall boundary layers,[6,7] transitional boundary layers,[8–10] airfoils,[11] high-lift devices,[12] shock-wave-boundary-layer interactions,[13,14] the transonic bump,[15,16] the NASA common research model,[17] etc.

In this work, we consider WMLES of turbulence in a spanwise rotating channel. Flow in a rotating frame of reference is encountered in, e.g., geophysics and turbomachinery applications. In this work, we will study the channel with spanwise rotation, which is a simple model problem for flow in rotating frames of reference. Figure 2 shows a schematic of a spanwise rotating channel. The system rotation is in the positive $z$ direction, leading to high pressure at the bottom wall and low pressure at the top wall, where are referred

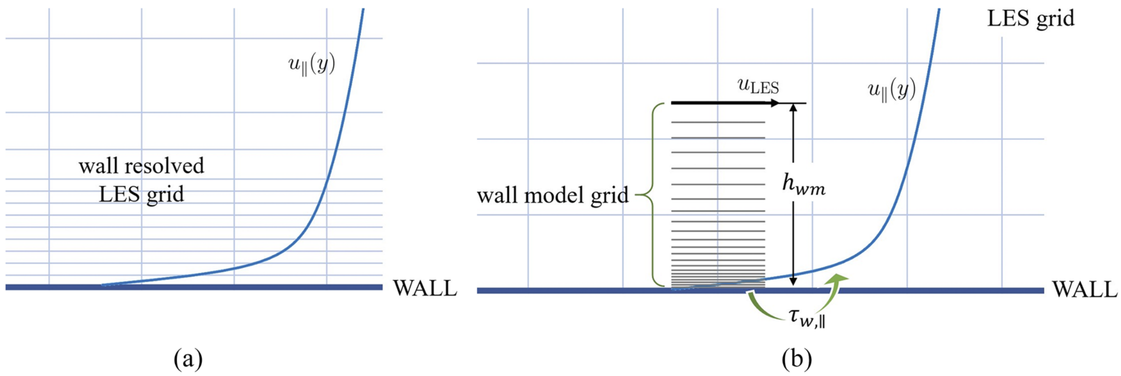


**FIG. 1**. Schematics of the typical setup of (a) a wall-resolved LES (WRLES) and (b) a WMLES.

to as the "pressure side" and the "suction side," respectively. Turbulence is enhanced near the pressure side and is suppressed near the suction side. The flow is controlled by two non-dimensional parameters, i.e., the Reynolds number $Re_\tau \equiv u_\tau h/\nu$ and the rotation number $Ro_\tau \equiv 2\Omega h/u_\tau$, where $h$ is the half channel height, $u_\tau = \sqrt{\tau_w/\rho}$ is the friction velocity, $\tau_w$ is the mean wall-shear stress, and $\rho \equiv 1$ is the fluid density.

Studies of this flow date back to the 1970s. Johnston *et al.*[18] conducted laboratory experiments of spanwise rotating channels. Detailed measurements show that, for flows at a high angular velocity, the mean velocity near the pressure side follows a linear scaling with a slope of $dU/dy = 2\Omega$. Here, $U$ is the mean velocity, $y$ is the distance from the wall, and $\Omega$ is the angular velocity. Later, laboratory experiments by Nakabayashi and Kitoh showed that the mean velocity deviates from the logarithmic law of the wall from $y \approx K_2\delta_c$, where $K_2$ is a constant and $\delta_c = u_\tau/|\Omega|$.[19] There were no direct numerical simulations (DNSs) of spanwise rotating channels until the 1990s.[20] To date, the DNSs in Refs. 21–23 cover $Re_\tau$ ranging from 117 to 1505 and $Ro_\tau$ ranging from 0 to 269. The authors showed that the flow becomes less turbulent as $Ro_\tau$ grows[24,25] and that large-scale roll cells emerge in spanwise rotating channels.[26,27]

System rotation modifies the flow physics. This poses challenges to modeling, specifically, to Reynolds-averaged Navier-Stokes

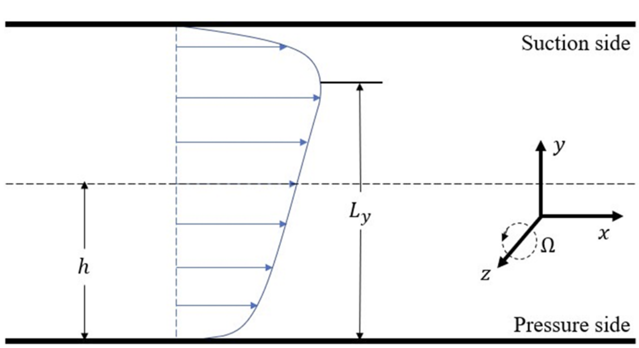


**FIG. 2**. A sketch of a spanwise rotating channel. The streamwise, wall-normal, and spanwise directions are denoted as *x*, *y*, and *z*.

(RANS)[28,29] and LES. To account for system rotation, Piomelli and Liu[30] included a time-dependent term in the dynamic eddy-viscosity model coefficient; Lamballais and Lesieur[31] developed a spectral-dynamic model and explicitly included the Coriolis term; and Silvis *et al.*[32] included a rotation-induced nonlinear term in the minimum-dissipation model,[33] just to name a few. Compared with subgrid scale (SGS) modeling, wall modeling has received much less attention. To the best of our knowledge, the only work is by Loppi *et al.*[34] In their work, the authors modified the eddy viscosity formulation in the equilibrium wall model by calibrating their model with wall-resolved large eddy simulations (WRLESs). (We will present details of their model in Sec. II B.)

In this work, we will develop a wall modeling capability. We will follow the conventional practice and resort to the known mean flow scaling near the pressure side[35]

$$U^+ = \frac{y^+}{l_\Omega^+} + \frac{1}{\kappa}\log(l_\Omega^+), \tag{1}$$

where $\kappa \approx 0.4$ is the von Kármán constant, $l_\Omega \equiv u_{\tau,p}/2\Omega$ is a rotation-induced length scale, and the superscript "+" denotes normalization using viscous units on the pressure side. Hereon, we will use subscripts $p$ and $s$ to denote quantities evaluated near the pressure and the suction sides, respectively. By definition, $l_\Omega^+ \equiv u_{\tau,p}^2/2\Omega\nu = Re_{\tau,p}/Ro_{\tau,p}$. Similar to the equilibrium wall model, knowing the LES velocity $u_\parallel$ at an off-wall location $h_{wm}$, one could use the above equation to compute the wall-shear stress $\tau_w = \rho u_{\tau,p}^2$ at the pressure side (iteratively). In addition to imposing the law of the wall locally and instantaneously, we will also pursue a data-based approach, where we train a feed-forward neural network (FNN) using the available DNS data and employ the trained FNN as a wall model in our LES.

The rest of this paper is organized as follows: Details of the wall models are presented in Sec. II. We also compare our models with the equilibrium wall model and the model in Ref. 34. In Sec. III, we present details of our computational setup. The results are presented in Sec. IV, followed by concluding remarks in Sec. V.

## II. WALL MODELING

In this section, we will briefly review the equilibrium wall model and the model in Ref. 34. For brevity, we will refer to the model in

Ref. 34 as the LBD model. Then, we will present details of our law-of-the-wall-based model and our data-based model. In anticipation of the results in later sections, we will also briefly review two remedies of log-layer mismatch (LLM) toward the end of this section.

### A. Equilibrium wall model

The equilibrium wall model models the near-wall turbulence through the following simplified thin-boundary-layer equation:

$$\frac{\mathrm{d}}{\mathrm{d}y}\left((\nu+\nu_T)\frac{\mathrm{d}u_\parallel}{\mathrm{d}y}\right)=0, \tag{2}$$

where $u_\parallel$ is the wall-parallel velocity, $\nu$ is the molecular viscosity, and $\nu_T$ is the eddy viscosity, which is modeled according to Prandtl's mixing length model as

$$\nu_T = l_m u_\tau D(y^+), \tag{3}$$

where $l_m = \kappa y$ is the Prandtl mixing length and $D(y^+)$ is the van Driest damping function expressed as[36]

$$D(y^+) = \left[1-\exp\left(-\frac{y^+}{A^+}\right)\right]^2, \tag{4}$$

where the constant is $A^+ = 17$. The boundary conditions of Eq. (2) are

$$u_\parallel(y=0)=0,\quad u_\parallel(y=h_{wm})=u_{\mathrm{LES}}, \tag{5}$$

where the no-slip boundary condition is applied at the wall and a matching condition is applied at the off-wall location $h_{wm}$, at which height the wall model velocity matches with the LES velocity $u_{\mathrm{LES}}$ (see Fig. 1).

Solving the model equations, the equilibrium wall model leads to logarithmic velocity profiles. Comparing these solutions with the DNS in Fig. 3, we see that the equilibrium wall model does not work well for flow in a spanwise rotating channel. The above consideration motivated the LBD model.

### B. LBD wall model

Admitting that the logarithmic law of the wall is not a good working approximation of the mean flow in a spanwise rotating channel, Loppi *et al.*[34] proposed to use a different eddy viscosity formulation

$$\nu_{T,L} = (l_m C_L) u_\tau D_L(y^+), \tag{6}$$

where $l_m = \kappa y$ is the conventional Prandtl mixing length, $D_L$ is the damping function expressed as

$$D_L(y^+) = \left[1-\exp\left(-\frac{y^+}{A_L^+}\right)\right]^2, \tag{7}$$

and $C_L$ is a rotation-induced correction term expressed as

$$C_L = 1-\beta Ri, \tag{8}$$

where $Ri$ is the gradient Richardson number expressed as

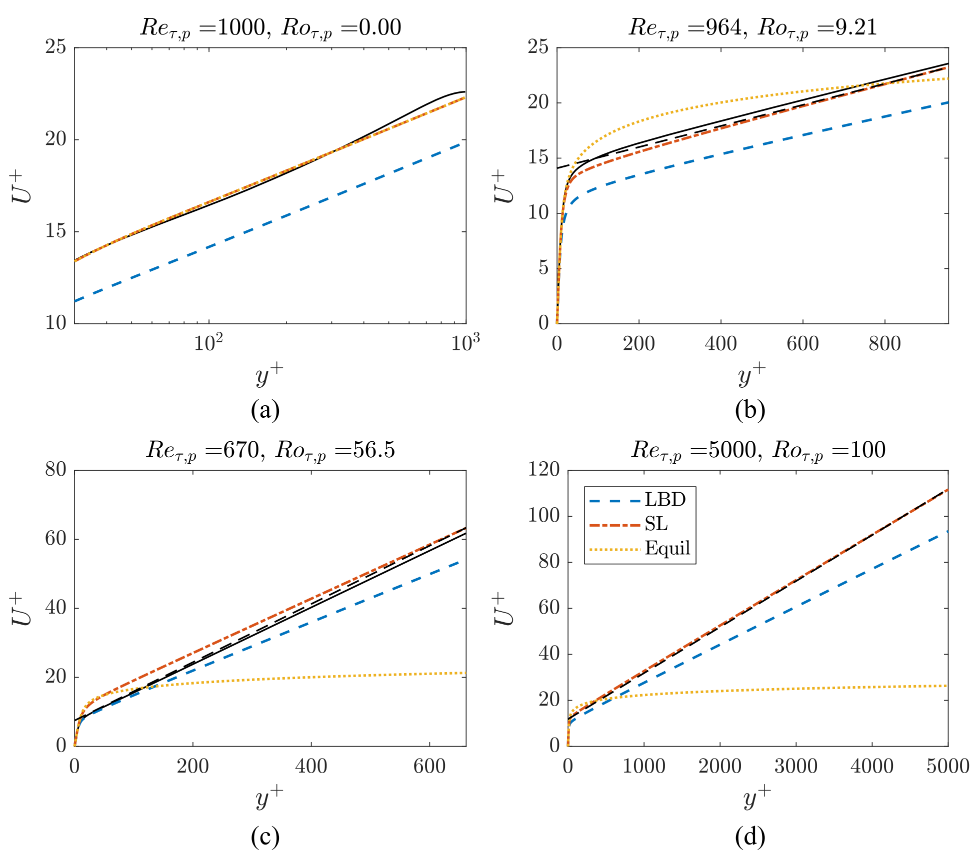


**FIG. 3**. Solutions of the equilibrium wall model, the LBD model, and the SL model at friction Reynolds numbers $Re_{\tau,p}$ = 1000, 964, 670, and 5000 and friction rotation numbers $Ro_{\tau,p}$ = 0, 9.21, 56.5, and 100 in (a)–(d), respectively. We use colored dashed lines for wall model solutions, black solid lines for DNS in (a)–(c), and black dashed lines for Eq. (1) in (b)–(d). The SL model reduces to the equilibrium wall model at 0 rotation number. Note that these are solutions of the wall model ODE, but not solutions of WMLES.

$$Ri = S(S+1), \tag{9}$$

where

$$S = -\frac{2\Omega}{\mathrm{d}u_\parallel/\mathrm{d}y}. \tag{10}$$

Because $Ri = 0$ for nonrotating channels, the above eddy viscosity formulation could be regarded as a truncated Taylor expansion at $Ri = 0$, where only the first term, i.e., $\beta Ri$, is retained.

Loppi *et al.* calibrated the constants $\beta$ and $A_L^+$ against a WRLES at a bulk Reynolds number $Re_b = 20\,000$ and a bulk rotation number $Ro_b = 0.45$. The above condition corresponds to $Re_{\tau,p} = 1062$ and $Ro_{\tau,p} = 8.47$. Here, $Re_b = U_b h/\nu$ and $Ro_b = 2|\Omega|h/U_b$, where $U_b$ is the bulk velocity. Loppi *et al.* got $\beta = 3.6$, $A_{L,p}^+ = 11$ at the pressure side, and $A_{L,s}^+ = 80$ at the suction side.

The above LBD model works well at flow conditions near the Reynolds number and the rotation number it is calibrated for, but because the calibrated $A_L^+$ does not equal the van Driest damping constant $A^+$, the model does not recover the equilibrium wall model at $\Omega = 0$. Moreover, the model does not yield the linear mean flow scaling Eq. (1) at high rotation numbers. To see that, we first integrate Eq. (2) and evaluate the integrated equation at the wall as follows:

$$(\nu + \nu_{T,L})\frac{\mathrm{d}u_\parallel}{\mathrm{d}y} = \tau_w. \tag{11}$$

Second, we substitute Eqs. (6)–(10) in Eq. (11),

$$\left\{\nu + l_m u_\tau D_L\left[1 + \beta\frac{2\Omega}{\mathrm{d}u_\parallel/\mathrm{d}y}\left(1 - \frac{2\Omega}{\mathrm{d}u_\parallel/\mathrm{d}y}\right)\right]\right\}\frac{\mathrm{d}u_\parallel}{\mathrm{d}y} = \tau_w, \tag{12}$$

which leads to

$$\left(1 + \frac{\nu}{l_m u_\tau D_L}\right)\left(\frac{\mathrm{d}u_\parallel}{\mathrm{d}y}\right)^2 + \left(\beta\cdot 2\Omega - \frac{\tau_w}{l_m u_\tau D_L}\right)\frac{\mathrm{d}u_\parallel}{\mathrm{d}y} - \beta\cdot(2\Omega)^2 = 0. \tag{13}$$

Next, we evaluate the above equation at the pressure side and normalize it using wall units as follows:

$$\left(1 + \frac{1}{\kappa y^+ D_L}\right)\left(\frac{\mathrm{d}u_\parallel^+}{\mathrm{d}y^+}\right)^2 + \left(\beta\cdot\frac{Ro_{\tau,p}}{Re_{\tau,p}} - \frac{1}{\kappa y^+ D_L}\right)\frac{\mathrm{d}u_\parallel^+}{\mathrm{d}y^+} - \beta\cdot\frac{Ro_{\tau,p}^2}{Re_{\tau,p}^2} = 0. \tag{14}$$

Last, we evaluate the above equation at a sufficiently large $y^+$, where the mean flow follows the linear scaling and $\mathrm{d}u_\parallel/\mathrm{d}y = \gamma\cdot 2\Omega$, i.e., $\mathrm{d}u_\parallel^+/\mathrm{d}y^+ = \gamma\cdot Ro_{\tau,p}/Re_{\tau,p}$, and the damping function $D_L \approx 1$. Here, $\gamma$ is a constant parameter, which is 1 in experiments and DNSs. This leads to

$$\gamma^2 + \beta(\gamma - 1) + \frac{1}{\kappa y^+}\left(\gamma^2 - \gamma\frac{Re_{\tau,p}}{Ro_{\tau,p}}\right) = 0. \tag{15}$$

The above equation does not hold for any nonzero value of $\gamma$. Also, one could integrate Eqs. (6)–(11) and compare the integrated velocity with DNS. In Figs. 3(a)–3(c), we compare the solutions of Eqs. (6)–(11) with the DNSs[23] at friction Reynolds numbers $Re_{\tau,p}$ = 1000, 964, and 670 and friction rotation numbers $Ro_{\tau,p}$ = 0, 9.21, and 56.5, respectively. At zero rotation [$Ro_{\tau,p} = 0$, Fig. 3(a)], because of the use of a different damping constant than the conventional van Driest damping constant, the LBD model predicts a constant downward shift with respect to the data. At a moderate rotation number [$Ro_{\tau,p} = 9.21$, Fig. 3(b)], the LBD model captures the linear mean flow behavior and the predicted velocity gradient agrees reasonably well with the data, but a constant downward shift in the mean velocity with respect to the DNS is found (note that this is the result of analytical integration, and therefore, the downward shift is not a consequence of log-layer mismatch). At a high rotation number [$Ro_{\tau,p} = 56.5$, Fig. 3(c)], the LBD model captures the linear mean flow behavior, but the predicted velocity gradient is slightly different from $2\Omega$. Last, if we further increase the friction Reynolds number and the rotation number [$Ro_{\tau,p} = 100$, Fig. 3(d)], the mean velocity according to the LBD model deviates further from the expected linear scaling at large $y^+$ values.

To briefly summarize, spanwise rotation modifies the flow physics, and the eddy viscosity has to be modified accordingly to account for system rotation; Loppi *et al.*[34] modified the eddy viscosity formulation by including a rotation-induced factor; the resulting model correctly captures the linear behavior of the mean flow at high rotation numbers as well as the logarithmic behavior of the mean flow at low rotation numbers; but the predicted mean velocity profiles are not entirely consistent with the data. This motivates the present work and the development of the "simple linear" model, i.e., the simple linear (SL) model.

### C. The SL model

In this subsection, we develop a new model for the flow in the wall layer. We start by writing down the time-averaged streamwise momentum equation. The mean flow in a spanwise rotating channel is unidirectional. The mean velocity $U(y)$ is governed by the following equation:

$$0 = -\frac{1}{\rho}\frac{\mathrm{d}P}{\mathrm{d}x} + \nu\frac{\mathrm{d}^2U}{\mathrm{d}y^2} - \frac{\mathrm{d}\langle u'v'\rangle}{\mathrm{d}y}, \tag{16}$$

where the pressure term contains the centrifugal potential. The equation is formally no different from that in a nonrotating channel. Equation (2) is therefore a good starting point for wall modeling. This is also why Loppi *et al.*[34] did not use a different model form. Following Ref. 34, we will work with Eq. (2) as well.

Defining $l_\Omega = u_{\tau,p}/2\Omega$, Yang *et al.*[35] suggested that the mixing length is

$$\begin{aligned} l_{m,\mathrm{Log}} &= \kappa y, \quad \text{for} \quad 1 \ll y^+, y \ll l_\Omega/\kappa, \\ l_{m,\mathrm{Lin}} &= l_\Omega, \quad \text{for} \quad y \gg l_\Omega/\kappa, \end{aligned} \tag{17}$$

in a spanwise rotating channel. Thus-defined mixing length is continuous in $y$ and leads to a linear mean velocity profile with a slope of $2\Omega$ at high rotation numbers and a logarithmic mean velocity profile at low rotation numbers. However, Eq. (17) suffers from two weaknesses. First, the mixing length abruptly changes from $l_m = \kappa y$ to a constant $l_m = l_\Omega$: this is numerically unstable. Second, for flows at low rotation numbers, Eq. (17) is no different from Eq. (3), and the flow is agnostic about system rotation.

We deal with the first weakness by taking the harmonic mean of $l_{m,\mathrm{Log}}$ and $l_{m,\mathrm{Lin}}$,

$$l_{m,\mathrm{Har}} = \left(\frac{1}{\kappa y} + \frac{1}{l_\Omega}\right)^{-1}. \tag{18}$$

The above mixing length and its derivative are continuous in $y$. At low rotation numbers, $l_\Omega$ is large and $l_{m,\mathrm{Har}} \approx \kappa y$ is the Prandtl mixing length. At high rotation numbers, $l_\Omega$ is small and $l_{m,\mathrm{Har}} \approx l_\Omega$. Equation (18) is a modeling choice and a trade-off between simplicity and accuracy. In general, one could take the $n$th harmonic mean, i.e., $l_{m,\mathrm{Har}} = (1/(\kappa y)^n + 1/l_\Omega^n)^{-1/n}$, but for our purposes, Eq. (18) suffices. To deal with the second weakness, we follow Loppi *et al.*,[34] and Taylor expands the mixing length near $S = 0$ and keeps the first term

$$l_{m,\mathrm{Log2}} = \kappa y(1 - \alpha S), \tag{19}$$

where $\alpha = 7.0$ is a model parameter determined through best fits of the measured Reynolds stress. Again, in general, one could keep higher order terms, but to strike a balance between simplicity and accuracy, we only keep one term. In summary, our mixing length reads

$$l_{m,\mathrm{SL}} = \left[\frac{1}{l_{m,\mathrm{Log2}}} + \frac{1}{l_{m,\mathrm{Lin}}}\right]^{-1} = \left[\frac{1}{\kappa y(1 - \alpha S)} + \frac{2\Omega}{u_{\tau,p}}\right]^{-1}. \tag{20}$$

Equation (20) not only recovers the logarithmic law of the wall at low rotation numbers and Eq. (1) at high rotation numbers but also is numerically stable and accounts for deviations from the logarithmic scaling at low rotation numbers. The full wall model is given by Eqs. (2)–(5) and Eq. (20).

We have mostly followed Ref. 34, but compared with the LBD model, Eq. (20) has a few advantages. First, the mixing length leads to a linear mean profile with a $2\Omega$ slope at high rotation numbers. To see that, we evaluate the model at large $y^+$ and a large rotation number as follows:

$$\frac{\mathrm{d}}{\mathrm{d}y}\left(l_\Omega u_{\tau,p}\frac{\mathrm{d}u_\parallel}{\mathrm{d}y}\right) = 0. \tag{21}$$

If the mean flow is such that $\mathrm{d}u_\parallel/\mathrm{d}y = 2\Omega$, it is trivial that the above equation holds. Second, our wall model recovers the equilibrium wall model at 0 rotation number. To test the model in an *a priori* sense, one can integrate Eqs. (2), (5), and (20) and compare the solutions with DNS. The results are shown in Fig. 3. Compared with the LBD model, the present formulation provides more accurate predictions of the mean flow at both low and high rotation numbers. In the following, we will refer to our model as the "simple linear" (SL) model, as it has a simple form and recovers the linear model.

## D. Data-based wall models

In the above two subsections, we reviewed the model in Ref. 34 and proposed a new model for spanwise rotating channel flow. Both Loppi *et al.* and we have taken a physics-based modeling approach: we make physically plausible assumptions and test the resulting model by comparing the model to data. In such a physics-based approach, data are used to test and validate a model and therefore play a secondary role. In the recent literature, the data-based modeling approach, where data play a primary role, has received much attention.[37–39] Compared with physics-based models, if one has data, developing data-based models that directly relate inputs and outputs is usually more straight-forward from a conceptual standpoint, and the resulting models usually fit the data very well. (Certainly, data-based models are often criticized for not being able to answer questions that are not registered near the training dataset.)

In this subsection, we make use of the DNS data in Refs. 22 and 23 and take a data-based approach. A somewhat related work is Ref. 40, where the authors trained a feed-forward neural network using channel flow DNS data and employed the trained network as a wall model in WMLES of channel flow and 3D boundary-layer flow. Before we proceed with the model details, we provide some background knowledge about an artificial neural network. Figure 4 shows a sketch of an FNN. In an FNN, information in the input layer is fed forward through hidden layers and generates an output.

Following Ref. 40, we train an FNN to learn about the law of the wall in a spanwise rotating channel. The mean flow $U$ near the pressure side depends on the system rotation $\Omega$, the fluid viscosity $\nu$, the friction velocity $u_\tau$ ($u_{\tau,p}$), and the distance from the wall $y$. The half channel height $h$ is an outer scale and is not a part of the equation. This is like that in a nonrotating channel, where the near-wall flow depends on $u_\tau$, $\nu$, and $y$, but not $h$.[41] The most straight-forward and possibly the most inefficient training strategy is to use the dimensional variables $\Omega$, $\nu$, $u_\tau$, and $y$ as the network input and the mean flow $U$, which also carries dimension, as the network output. A slightly more efficient strategy is to group the dimensional variables into nondimensional groups and use the nondimensional groups as the network input. For a spanwise rotating channel, the Buckingham $\Pi$ theorem dictates that the four variables lead to two independent nondimensional groups. A straight-forward nondimensionalization leads to $y^+$ and $l_\Omega^+$, where $y^+$ is the viscous distance from the wall and $l_\Omega^+$ is the nondimensionalized rotation-induced length scale. Training using $y^+$ and $l_\Omega^+$ (alternatively, $l_\Omega^{+-1}$ to account for $\Omega = 0$) as our input and $U^+$ as our output, we take a "non-physics-informed" approach because we did not invoke any of our prior knowledge on the flow.

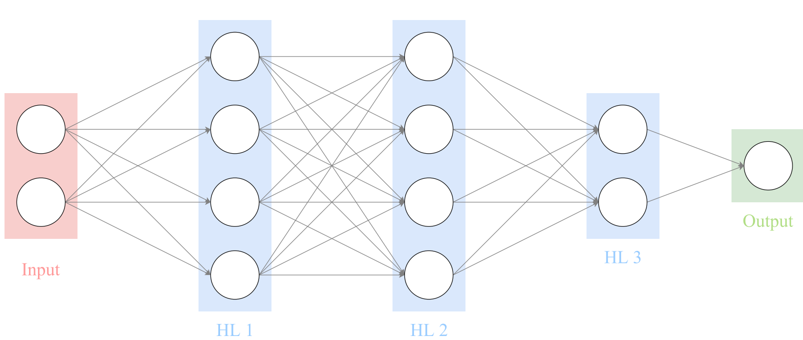


**FIG. 4.** A sketch of an FNN. The input layer contains two neurons. There are three hidden layers with 4, 4, and 2 neurons, respectively. The output layer contains one neuron.

If nothing was known about the flow, invoking the Π theorem and taking the non-physics-informed approach are probably the only thing we could do. However, for the problem of the spanwise rotating channel, we know approximately how the mean flow behaves. By informing the neural network about this knowledge, we could take a "physics-informed" approach. The basic idea is to regroup the nondimensional input and output variables such that the functional dependence between the input and the output becomes "simple." Depending on the tool we use, the definition of "simple" may well vary. For FNNs, usually, a linear dependence is considered to be simple and a logarithmic dependence is considered to be less simple. For example, if we were to model the mean flow in a channel, where $U^+ \sim \log(y^+)$ in the logarithmic layer, it would be more efficient to use $\log(y^+)$ as the input and $U^+$ as the output than to directly use $y^+$ as the input and $U^+$ as the output. Alternatively, one could use $y^+$ as the input and $U - \log(y^+)/\kappa$ as the output. From the above example, it is probably also clear that there is more than one way one could inform the neural network about the known physics (which is the reason why training a neural network is also an art[42]). Here, we use

$$y^+/l_\Omega^+$$

and

$$y^+$$

as our input and

$$U^+ - g(y^+, l_\Omega^+)$$

as the output, where

$$g(y^+, l_\Omega^+) = \frac{1}{\kappa}\log(y^+) H\left(-y^+ + \frac{l_\Omega^+}{\kappa}\right) + \left[\frac{y^+}{l_\Omega^+} + \frac{1}{\kappa}\log(l_\Omega^+) - \frac{1}{\kappa}\log(\kappa e)\right] H\left(y^+ - \frac{l_\Omega^+}{\kappa}\right),$$

where $H$ is the Heaviside function expressed as

$$H(x) = 0, \text{ if } x < 0 \\ H(x) = 1, \text{ if } x \geq 0, \tag{22}$$

and $e$ is the base of the natural logarithm. The function $g$ is a fairly rough scaling estimate of the mean flow in a spanwise rotating channel.[35] It transitions continuously from being logarithmic to being linear. The term $\log(\kappa e)$ is included so that $g$ is continuous at $y^+ = l_\Omega^+/\kappa$. Again, there is more than one way we could inform a neural network about our knowledge on the flow physics, and this is just one of the many possibilities.

The mean flow data in Refs. 22 and 23 are the training data. The dataset includes various combinations of Reynolds numbers and rotation numbers and covers a Reynolds number range from $Re_\tau = 180$ to $Re_\tau = 1500$ and a rotation number range from $Ro_\tau = 0$ to $Ro_\tau = 270$. The data in the viscous sublayer are precluded—if the viscous sublayer is resolved in a WMLES, one would not have to use a wall model. The data near the suction side are excluded from the training as well because the flow is close to laminar near the suction side. The training data size is fairly small, containing only about 5000 pairs of input and output.

Considering that a wall model is evaluated at every wall location and at every time step, the cost of evaluating the neural network is an equally important consideration as its accuracy. For the FNNs here, we start from a sufficiently large neural network and reduce its size until we could not get an accurate prediction. The size of the two FNNs is 4, 4, and 2, i.e., three hidden layers with 4, 4, and 2 neurons in each layer. The weights and biases are randomly initialized. The training converges after about 10 000 epochs, which takes about 1 min or so on a desktop. Table I tabulates the details of the two FNNs.

**TABLE I.** The network size, the input, and the output of the feed-forward neural network. NN1 is non-physics-informed. NN2 is physics-informed.

| NN | Hidden layer size | Input | Output |
|---|---|---|---|
| NN1 | 4, 4, 2 | $y^+, l_\Omega^{+-1}$ | $U^+$ |
| NN2 | 4, 4, 2 | $y^+, y^+/l_\Omega^+$ | $U^+ - g$ |

In Fig. 5, we compare the network to data. For flow parameters within the training data, i.e., Figs. 5(a)–5(c), both NN1 and NN2 work well. For flow parameters outside the training data, i.e., Fig. 5(d), only NN2, the physics-informed neural network, is able to predict the expected mean flow.

### E. Log-layer mismatch remedies

Log-layer mismatch (LLM) is a chronic problem for near-wall turbulence modeling and is found in WMLES, hybrid RANS/LES,[43] and DES.[44] LLM occurs when the wall model matches with the LES solution at the first off-wall LES grid. It leads to $\mathcal{O}(10\% - 20\%)$ error in the predicted wall-shear stress in boundary layer flow calculations and $\mathcal{O}(10\% - 20\%)$ error in the predicted flow rate in channel and pipe flow calculations (where the pressure gradient is kept constant).

The mechanism behind the LLM has received much attention. Kawai and Larsson[45] argued that because the near-wall turbulent eddies are not well-resolved, the near-wall LES solution is "contaminated." Resultantly, in order to fix the LLM problem, one needs to use the LES velocity at a grid point further away from the wall, where the LES solution is not "contaminated." The typical implementation of the above remedy involves the use of the third off-wall grid point, and thus, this remedy is commonly known as the "third grid point fix." The "third grid point fix" proves to work well for simple geometries, but in practice, computing the local wall-shear stress using the velocity at a grid point away from the wall is not always computationally efficient. Yang *et al.*[46] interpreted the LLM differently. The authors decomposed the modeled instantaneous shear stress into its mean and a fluctuating part

$$\tau_{\rm wm} = \langle \tau_{\rm wm} \rangle + C\rho u_\tau U'_{\rm LES}. \tag{23}$$

It is clear from the above equation that the instantaneous fluctuations of the wall-shear stress are locked with the instantaneous stream velocity fluctuations at the wall-model/LES matching location. The authors argued that LLM occurs when this lock is between the wall-shear stress and the velocity at the first off-wall grid point. Here, $C$ is a wall-model-dependent coefficient. To remove LLM, one only needs to break this lock. Following the above argument to its logical conclusion, the "third grid point remedy" breaks the lock between the wall-shear stress and the first off-wall LES velocity, and

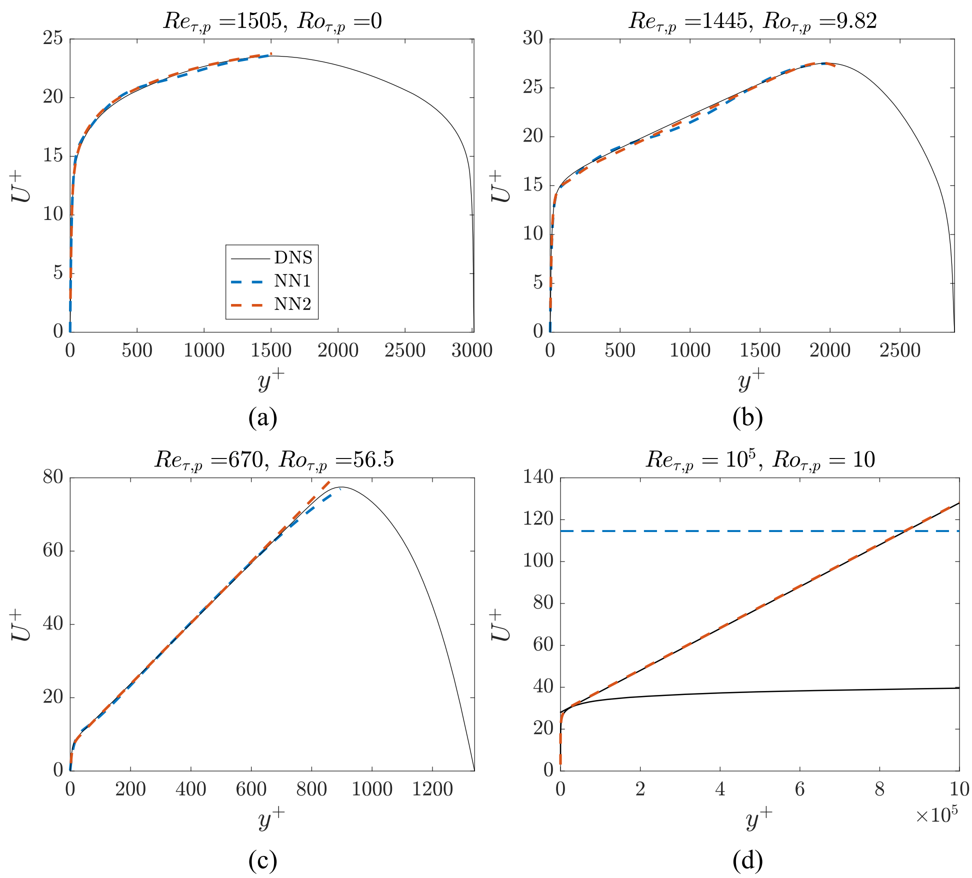


**FIG. 5**. Predictions of the two neural networks and the DNS: (a) $Re_{\tau,p}$ = 1505, $Ro_{\tau,p}$ = 0.0, (b) $Re_{\tau,p}$ = 1445, $Ro_{\tau,p}$ = 9.82, (c) $Re_{\tau,p}$ = 670, $Ro_{\tau,p}$ = 56.5, and (d) $Re_{\tau,p} = 10^5$, $Ro_{\tau,p}$ = 10. The solid lines in (a)–(c) show the DNS results. The solid lines in (d) show the logarithmic law and the linear law.

therefore, this is a viable remedy for LLM. In order to compute the local wall-shear stress using the first off-wall grid, Yang *et al.* proposed to filter the LES velocity and use the filtered velocity as the wall model input, which was also found to work well for WMLES. It is also worth mentioning that the filtration technique was also adopted in Ref. 47 for WMLES of atmospheric boundary layer flows, although the technique is meant to reduce the difference between $\langle u^2\rangle$ and $\langle u\rangle^2$ such that the model predicted wall-shear stress is consistent with the real wall-shear stress. Aside from WMLES, LLM is also encountered in DES and hybrid RANS/LES and can be removed by adding a forcing term to the RANS equations,[48] by modifying the eddy viscosity at the RANS/LES interface,[49] or by constraining the subgrid stresses.[50]

In the following, we test if LLM persists in WMLES of spanwise rotating channels. Figure 6 shows the mean velocity profiles in WMLESs of spanwise rotating channels. The wall model in Subsection II C is used. The wall model matches with the LES at the first off-wall grid. We compare results with and without filtering the velocity at the first off-wall grid. LLM is found in WMLES of a nonrotating channel. Increasing slightly the rotation number, the mean flow still follows a logarithmic scaling and LLM persists. This is expected. LLM vanishes at high rotation numbers. In Figs. 6(c) and 6(d), where $Ro_{\tau,p} \gtrsim 10$, LLM could not be found, and it makes no difference if we filter or not filter the velocity at the first off-wall grid. In conclusion, LLM does not seem to be much of a problem for WMLES of the spanwise rotating channel, at least when the rotation number is high.

### F. A few additional details and remarks

Wall modeling is a very different field than subgrid scale modeling, and RANS is a very different tool than LES. Hence, lessons learned from subgrid scaling modeling and RANS modeling do not necessarily apply to wall modeling. In the previous literature, data-based approaches have mainly been used for SGS modeling and RANS modeling,[51] in which applications, writing model variables as tensors is beneficial. Invariants of tensors are insensitive to coordinate transformation, and this helps the network training. This lesson, however, has little relevance to wall modeling. In fact, while SGS models are often written in tensor forms,[52] wall models are rarely written in tensor forms.[3] The reason is that the wall normal direction and the direction of the near-wall velocity define an intrinsic coordinate system, and one defines all flow quantities in that coordinate system.

In our WMLESs, we will match the wall model with the LES at both the first and the third off-wall grids, and we will compare the simulation results. When the wall model interfaces with the LES at the first off-wall grid, the LES velocity is filtered. When the wall

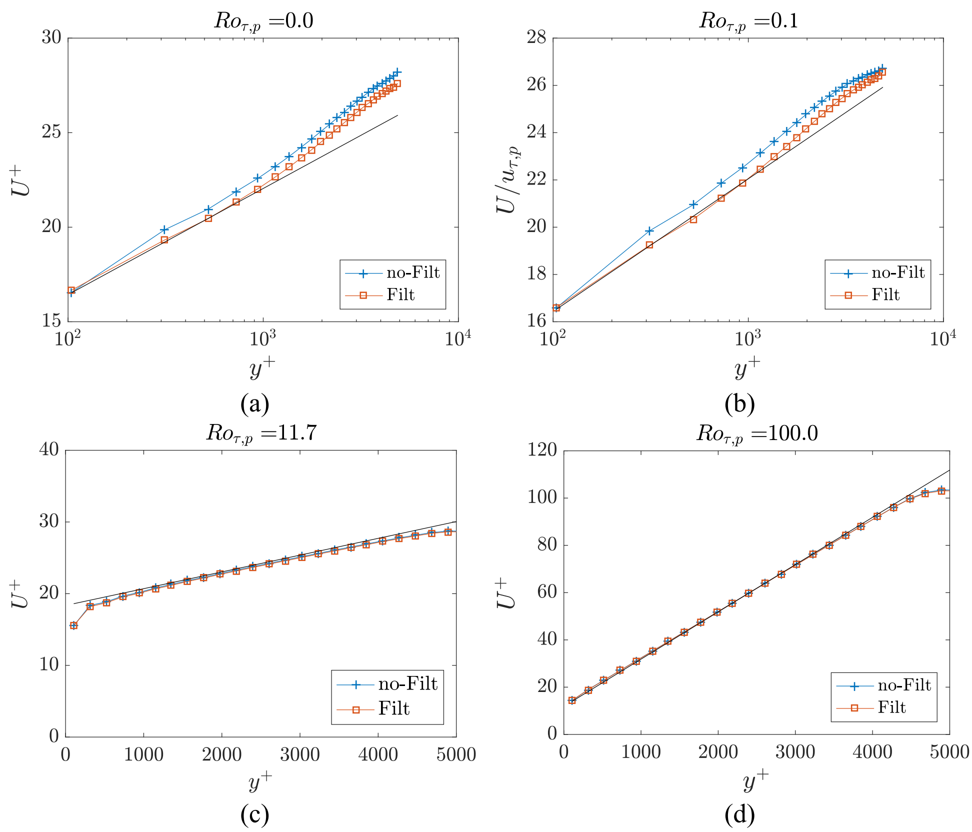


**FIG. 6**. Mean velocity profiles in WMLESs of spanwise rotating channels at $Re_{\tau,p}$ = 5000 with and without filtering the LES velocity at the first off-wall grid. (a) $Ro_{\tau,p}$ = 0.0. (b) $Ro_{\tau,p}$ = 0.1. (c) $Ro_{\tau,p}$ = 11.7. (d) $Ro_{\tau,p}$ = 100.0. The results are WMLES results.

model interfaces with the LES at the third off-wall grid, the LES velocity is directly fed to the wall model.

In the first three subsections, the wall models are in the form of a set of ODEs. It is not uncommon to use wall models in an algebraic form. For spanwise rotating channels, if the first off-wall grid is in the linear layer, then the following algebraic model could be used:

$$\frac{\tau_{w,\parallel}}{\rho} = u_{\tau,p}^2 = \left[\frac{\kappa(u_\parallel - 2\Omega y)}{\log(l_\Omega^+)}\right]^2. \tag{24}$$

Note that $\rho \equiv 1$ for all cases.

SGS models in LES are known to have difficulties with laminarization.[53] Because of the inadequacy of SGS models, the wall-shear stresses in the WRLES[34] do not agree with the stresses in the DNS.[23] In order to focus on the wall modeling aspect of the problem, we conduct WMLES of the "half channel," where we only simulate the flow near the pressure side. Similar to previous calculations, a symmetric boundary condition is imposed at the top boundary. To justify the use of the symmetric boundary condition, we examine the vertically integrated, time averaged, and horizontally averaged streamwise momentum equation as follows:

$$\langle u'v'\rangle = -\frac{\mathrm{d}P}{\mathrm{d}x}y - u_{\tau,p}^2 + \nu\frac{\mathrm{d}U}{\mathrm{d}y}. \tag{25}$$

At the top of the half channel, $\mathrm{d}U/\mathrm{d}y = 0$. The pressure force is balanced by the wall-shear stress, and therefore, $-\frac{\mathrm{d}P}{\mathrm{d}x}y - u_{\tau,p}^2 = 0$. Resultantly, $\langle u'v'\rangle = 0$. Hence, a symmetric boundary condition is a valid boundary condition at the top of the computational domain. Note that the above analysis is based on the Navier-Stokes equation and therefore is exact.

For all WMLESs, we use the wall-parallel velocity to compute the wall-shear stress. The computed wall-shear stress is then projected to the direction of the wall parallel velocity, i.e.,

$$\tau_{w,x} = \tau_w\frac{u_{\mathrm{LES}}}{\sqrt{u_{\mathrm{LES}}^2 + w_{\mathrm{LES}}^2}}, \quad \tau_{w,z} = \tau_w\frac{w_{\mathrm{LES}}}{\sqrt{u_{\mathrm{LES}}^2 + w_{\mathrm{LES}}^2}}. \tag{26}$$

## III. COMPUTATIONAL SETUP

A sketch of the computational domain is shown in Fig. 7. The flow subjects to spanwise rotation, and the angular velocity is $\Omega$. The streamwise, wall-normal, and spanwise directions are denoted as $x$, $y$, and $z$, respectively. The streamwise and the spanwise extents of the computational domain are $2\pi h$, where $h$ is the half channel height. A larger domain is used at a typical condition to ensure that our results do not depend on the domain size. The wall-normal extent of the computational domain is $L_y = u_{\tau,p}^2/u_\tau^2 h$. The wall-shear stress is balanced by the streamwise pressure gradient, and a stress-free condition is used at the top of the computational domain.

The solver LESGO is an open-source pseudospectral code. It solves the incompressible Navier-Stokes equations. Details of the code can be found in Refs. 54 and 55. Here, we only briefly summarize the main features of the code. A second-order finite

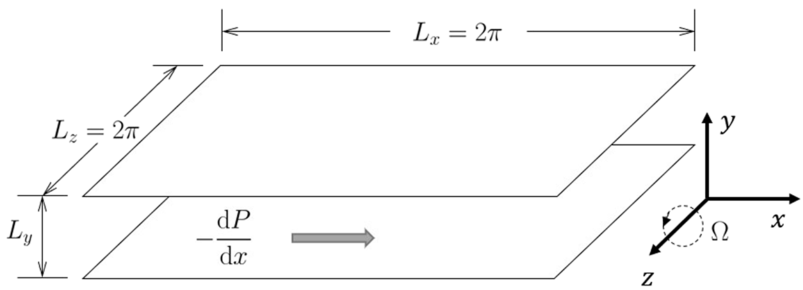


**FIG. 7**. A sketch of the computational domain. $x$, $y$, and $z$ are the streamwise, wall-normal, and spanwise directions. $L_x$, $L_y$, and $L_z$ are the streamwise, wall-normal, and spanwise extents of the computational domain. The flow is subject to a spanwise rotational speed $\Omega$ and is driven by a streamwise pressure gradient $-\dfrac{\mathrm{d}P}{\mathrm{d}x}$.

difference scheme is used in the wall-normal direction, and a spectrum method is used in the streamwise and the spanwise directions. The bottom boundary condition is given by a wall model, and a symmetric boundary condition is used at the top. Spanwise rotation leads to a Coriolis force. The subgrid scale stresses are modeled using the scale-dependent Lagrangian-dynamic Smagorinsky model.[54,56]

We conduct WMLESs at various Reynolds numbers and rotation numbers. Details of the WMLESs are tabulated in Table II. The $Re_\tau$ covers the range from 226 to 1505, and the $Ro_\tau$ covers the range from 0.0 to 67.4. $L_y = u_{\tau,p}^2/u_\tau^2 h$ is the wall-normal extent of our computational domain, which can be directly measured from the DNSs. The half channel height $h$ is 1. All cases use a 32 × 24 × 32 grid, and the grids are uniformly distributed in every direction. The friction Reynolds number, the friction rotation number, and their counterparts at the pressure side are also listed in Table II. The nomenclature of the cases is as follows: The cases are referred to as WM$_n$-Ro$_m$. "WM" is the wall model used and may be EQ, LBD, SL, ALG, NN1, or NN2, which correspond to the equilibrium wall model in Subsection II A, the LBD model in Subsection II B, the ordinary differential equation (ODE) model in Subsection II C, the algebraic model given by Eq. (24), and the non-physics-informed and the physics-informed neural network models in Subsection II D. "n" refers to the wall-model/LES matching location and may be 1 or 3, which correspond to the first or the third off-wall grid. "Ro" refers to the friction rotation number and is listed in the 5th column of Table II. We keep the digits before the decimal point for "Ro." $m$ is used to differentiate cases with the same wall model and the same rotation number. For example, SL$_1$-66 is a WMLES that uses the wall model in Sec. II C and the velocity at the first off-wall location as the wall model input, and $Ro_\tau$ = 66. In the following, we will also use part of the nomenclature to refer to more than one case. For example, we will use SL$_1$ to refer to all WMLESs that use the SL model and the velocity at the 1st off-wall point. Again, when velocity at the 1st

**TABLE II**. Details of the WMLESs. A total number of 88 WMLESs are conducted. In the first line, "SL$_{1,3}$, ALG$_{1,3}$, NN1$_1$, NN2$_1$-66" represents 6 cases: SL$_1$–66, SL$_3$–66, ALG$_1$–66, ALG$_3$–66, NN1$_1$–66, and NN2$_1$–66. $L_y$ is the wall-normal extent of our computational domain. This information is directly available from the DNS.[23] We use the wall models in Sec. II. "EQ" is the equilibrium wall model in Sec. II A, "LBD" is Loppi *et al.*'s model in Sec. II B, "SL" is our model in Sec. II C, "NN1" and "NN2" are the data-based models in Sec. II D, and "ALG" is the algebraic model in Sec. II E. The nomenclature of the cases is as follows: WM$_n$-Ro$_m$, where WM is the wall model used, $n$ is the wall-model/LES matching location, $Ro$ is the rotation number, and $m$ differentiates cases with the same wall model and the same rotation number. The subscript $p$ denotes quantities evaluated at the pressure side. The streamwise and the spanwise extents of the computational domains are $2\pi h$ for all WMLESs. All WMLESs use a 32 × 24 × 32 grid, which is a bit more generous than that of typical WMLES.[57,58]

| Case | $Re_{\tau,p}$ | $Ro_{\tau,p}$ | $Re_\tau$ | $Ro_\tau$ | $L_y$ | $l_\Omega^+$ |
|---|---|---|---|---|---|---|
| SL$_{1,3}$, ALG$_{1,3}$, NN1$_1$, NN2$_1$-66 | 249 | 60.4 | 226 | 66.5 | 1.22 | 4.15 |
| SL$_{1,3}$, ALG$_{1,3}$, NN1$_1$, NN2$_1$-43 | 325 | 37.0 | 277 | 43.4 | 1.37 | 8.77 |
| SL$_{1,3}$, ALG$_{1,3}$, NN1$_1$, NN2$_1$-56 | 501 | 47.9 | 423 | 56.7 | 1.40 | 10.48 |
| SL$_{1,3}$, ALG$_{1,3}$, LBD$_1$, NN2$_1$, NN1$_1$-67 | 670 | 56.5 | 562 | 67.4 | 1.42 | 11.84 |
| SL$_{1,3}$, ALG$_{1,3}$, NN1$_1$, NN2$_1$-26 | 416 | 21.6 | 339 | 26.5 | 1.50 | 19.23 |
| SL$_{1,3}$, ALG$_{1,3}$, NN1$_1$, NN2$_1$-33 | 677 | 26.6 | 544 | 33.1 | 1.55 | 25.47 |
| SL$_{1,3}$, ALG$_{1,3}$, NN1$_1$, NN2$_1$-34 | 988 | 28.8 | 822 | 34.6 | 1.44 | 34.30 |
| SL$_{1,3}$, ALG$_{1,3}$, NN1$_1$, NN2$_1$-18 | 851 | 15.3 | 700 | 18.6 | 1.48 | 55.67 |
| EQ$_{1,3}$, SL$_{1,3}$, ALG$_{1,3}$, NN1$_1$, NN2$_1$-10 | 535 | 8.37 | 435 | 10.3 | 1.51 | 63.93 |
| SL$_{1,3}$, ALG$_{1,3}$, LBD$_1$, NN2$_1$, NN1$_1$-11$_1$ | 964 | 9.21 | 800 | 11.1 | 1.45 | 104.59 |
| SL$_{1,3}$, ALG$_{1,3}$, NN1$_1$, NN2$_1$-11$_2$ | 1445 | 9.82 | 1213 | 11.7 | 1.42 | 147.03 |
| SL$_{1,3}$, ALG$_{1,3}$, NN1$_1$, NN2$_1$-3 | 1107 | 2.73 | 976 | 3.10 | 1.29 | 404.93 |
| SL$_{1,3}$, ALG$_{1,3}$, NN1$_1$, NN2$_1$-0$_1$ | 1000 | 0.00 | 1000 | 0.00 | 1.00 | ... |
| SL$_{1,3}$, ALG$_{1,3}$, NN1$_1$, NN2$_1$-0$_2$ | 1505 | 0.00 | 1505 | 0.00 | 1.00 | ... |

**TABLE III**. Details of the large domain WMLES. Here, "L" stands for a large domain.

| Case | $Re_{\tau,p}$ | $Ro_{\tau,p}$ | $Re_\tau$ | $Ro_\tau$ | $L_x \times L_y \times L_z$ | $N_x \times N_y \times N_z$ | $l_\Omega^+$ |
|---|---|---|---|---|---|---|---|
| $SL_1$-$11_1$L | 964 | 9.21 | 800 | 11.1 | $40\pi \times 1.45 \times 4\pi$ | $1280 \times 24 \times 128$ | 104.59 |

**TABLE IV**. Simulation details of high Reynolds number cases. Here, we use NN2 to model the wall-shear stresses. "C" stands for the coarse grid, and "R" stands for the refined grid.

| Case | $Re_{\tau,p}$ | $Ro_{\tau,p}$ | $Re_\tau$ | $Ro_\tau$ | $L_x \times L_y \times L_z$ | $N_x \times N_y \times N_z$ | $l_\Omega^+$ |
|---|---|---|---|---|---|---|---|
| $NN2_1$-71C | $5.07 \times 10^5$ | 50.7 | $3.61 \times 10^5$ | 71.2 | $3.94\pi \times 1.971 \times 3.94\pi$ | $32 \times 24 \times 32$ | $10^4$ |
| $NN2_1$-71R | $5.07 \times 10^5$ | 50.7 | $3.61 \times 10^5$ | 71.2 | $3.94\pi \times 1.971 \times 3.94\pi$ | $64 \times 48 \times 64$ | $10^4$ |
| $NN2_1$-7C | $5.09 \times 10^4$ | 5.09 | $3.63 \times 10^4$ | 7.13 | $3.93\pi \times 1.965 \times 3.93\pi$ | $32 \times 24 \times 32$ | $10^4$ |
| $NN2_1$-7R | $5.09 \times 10^4$ | 5.09 | $3.63 \times 10^4$ | 7.13 | $3.93\pi \times 1.965 \times 3.93\pi$ | $64 \times 48 \times 64$ | $10^4$ |

off-wall location is used, the LES velocity is filtered. The LBD model is used for two WMLESs: one at the flow condition that is close to the condition the model is calibrated for and the other at the flow condition that is slightly away.

We repeat $SL_1$-$11_1$ in a larger domain to confirm that the results are not dependent on the domain size. Details of this simulation are included in Table III. In addition, we conduct two additional WMLESs at $Re_{\tau,p} = 5.07 \times 10^5$ and $5.09 \times 10^4$. Details of the two cases are tabulated in Table IV. Both cases use the same grid point number as in the previous simulations, i.e., $32 \times 24 \times 32$.

## IV. RESULTS AND DISCUSSIONS

### A. Instantaneous flow features

Before presenting any flow statistics, we first take a brief look at the instantaneous flow fields in one case. In the following, we show the instantaneous velocities in $SL_1$-$11_1$L. This case has a moderate rotation number and a large computational domain ($L_x \times L_y \times L_z = 40\pi \times 1.45 \times 4\pi$).

Figure 8 shows the instantaneous streamwise velocity on a spanwise/wall-normal plane at an arbitrarily picked streamwise location. Compared with channel flow with no spanwise rotation, the flow is less well mixed. Figure 9 shows the instantaneous streamwise, spanwise, and wall-normal velocities at wall-normal locations $y/L_y = 0.125$, 0.25, and 0.5. All the three locations are in the linear layer. Streak-like structures are found in all contour plots. First, we compare the behavior of a velocity component at different wall-normal locations. For the streamwise velocity component, there are visibly fewer streaks at higher wall-normal locations. This is true for both channels with and without spanwise rotation. For the wall-normal component, the streaks become stronger as they move away from the wall. This is only observed in channels with spanwise rotation. For the spanwise component, a component that is not directly affected by system rotation, the streaks lose streamwise coherence away from the wall. Second, we compare velocity components. Both the spanwise and the wall-normal components are stronger than the streamwise component. The boundaries of the streaks are sharper in the streamwise and the wall-normal velocity contours than those in the spanwise velocity contours. The observations here are consistent with those in Ref. 23, and therefore, we could conclude that our LESs capture the overall flow features.

### B. Mean flow

Next, we show mean flow results. This will be our main test for the wall models.

First, we study the behavior of the equilibrium wall model. Following our discussion in Sec. II A, the logarithmic law of the wall is a poor approximation of the mean flow in a spanwise rotating channel, and if the equilibrium wall model is applied as is, the mean flow would likely be wrong. Here, we show the mean flow of $EQ_1$-10 and $EQ_3$-10 in Fig. 10. For flow at this condition, at a

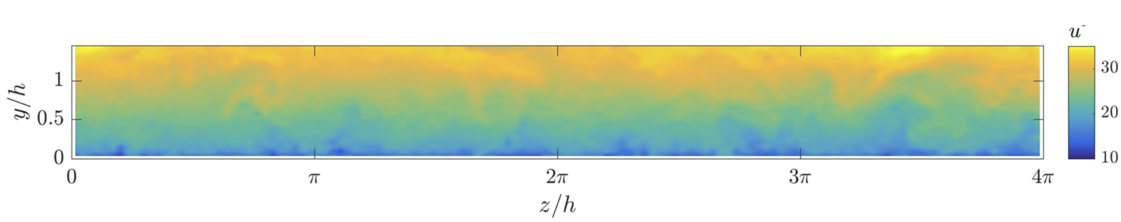


**FIG. 8**. Instantaneous streamwise velocity on a spanwise/wall-normal plane at an arbitrarily picked streamwise location in case $SL_1$-$11_1$L. Note that our computational domain is a half channel, as discussed in Sec. II F.

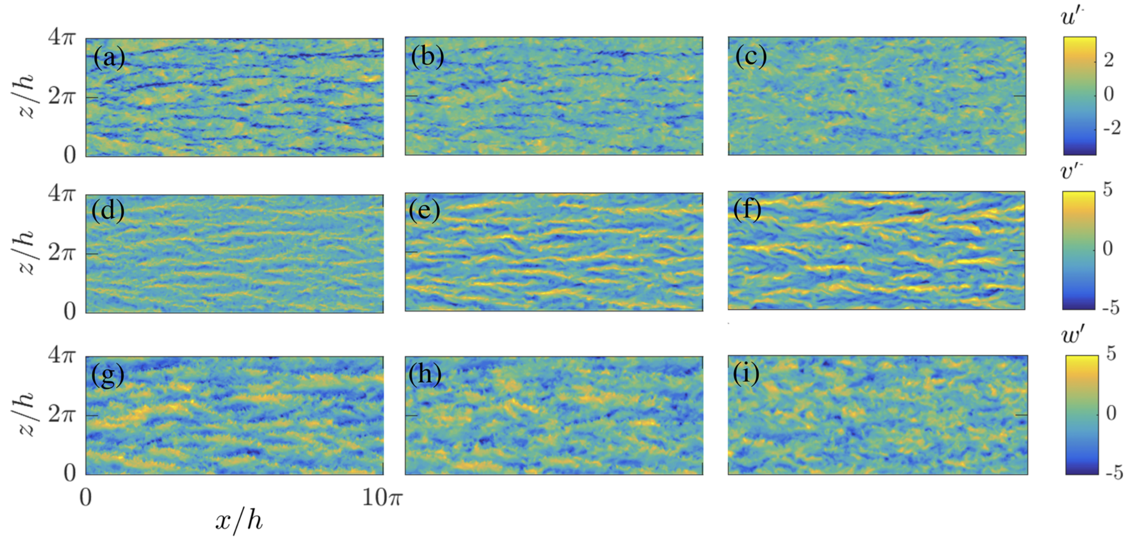


**FIG. 9**. Instantaneous contours on constant $y$ planes in case $SL_1$-$11_1$L: (a)–(c) streamwise velocity; (d)–(f) wall-normal velocity; (g)–(i) spanwise velocity. (a), (d), and (g) are at $y/L_y$ = 0.125, (b), (e), and (h) are at $y/L_y$ = 0.25, and (c), (f), and (i) are at $y/L_y$ = 0.5. Here, we have shown only part of the computational domain.

distance $\Delta z/2$ from the wall, i.e., at the first off-wall grid, the linear scaling and the logarithmic scaling yield the same velocity. Resultantly, $EQ_1$ gives a reasonably good mean flow prediction even though the equilibrium wall model is used. In general, the log law and the linear law give different velocities at the same wall-normal height—this is the case at the third grid point from the wall. In this case, results from $EQ_3$ do not agree with the DNS. Note that the discrepancy between the DNS here is solely due to the difference between the log law and the linear law, not the wall-model/LES matching location. If the two scalings cross at the distance $z = 2.5\Delta z$, i.e., at the third off-wall grid, $EQ_3$ would yield a good prediction and $EQ_1$ would be erroneous.

Second, we examine the LBD model. The model is used in two cases, i.e., $LBD_1$-67 and $LBD_1$-$11_1$. The results are shown in Fig. 11.

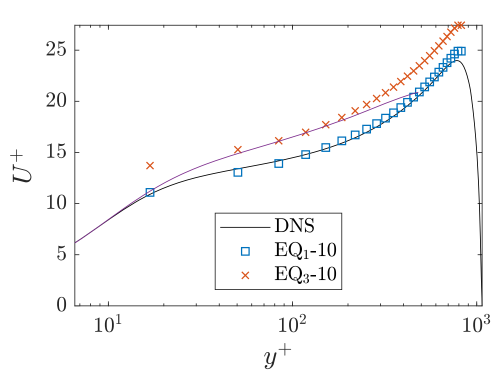


**FIG. 10**. Mean flows in $EQ_1$-10 and $EQ_3$-10 and their DNS counterpart. The purple line represents the mean flow in a nonrotating channel at the same Reynolds number. Again, we conduct WMLES in a half channel, as discussed in Sec. II F.

We compare the LBD model with the SL model. At $Ro_\tau$ = 67, both models work well. At $Ro_\tau$ = 11, the LBD model underpredicts the mean flow, whereas the SL model again works well. This confirms our analysis in Sec. II B: the LBD model works well at some flow condition but falls short when applied to other flow conditions.

Third, we examine the SL model. Figure 12 shows the mean flows of WMLESs that use the SL model. The figure includes results from $SL_1$, $SL_3$, and DNS. We compare $SL_1$ and $SL_3$, i.e., the first-grid point implementation and the third-grid point implementation. $SL_1$ works well at both low and high rotation numbers. There are deviations near the top of our half channels, e.g., in cases $SL_1$-26, $SL_1$-18, $SL_1$-33, and $SL_1$-43, but considering that we are simulating half channels instead of full channels, these deviations are not unexpected. $SL_3$ works well at low to moderate rotation numbers, i.e., for $Ro_\tau \lesssim 30$, but overpredicts the flow at high rotation numbers, i.e., $Ro_\tau \gtrsim 30$, leading to "linear layer mismatch." In Sec. II E, we have shown that "linear-layer mismatch" should not show up at high rotation numbers even if the wall model uses the unfiltered LES velocity at the first off-wall grid. We do not entirely know what may be responsible for the "linear layer mismatch" here. It will be a topic of interest for future investigations.

Next, we examine the performance of the algebraic models, i.e., $ALG_1$ and $ALG_3$. The results are shown in Fig. 13. The algebraic model imposes the linear scaling, i.e., Eq. (1), locally and instantaneously. Because the mean flow does not follow Eq. (1) at low rotation numbers, imposing the linear scaling at low rotation numbers will lead to errors. This is confirmed in Fig. 13(a), where both $ALG_1$ and $ALG_3$ underpredict the mean flow at low rotation numbers. At high rotation numbers, the mean flow follows the linear scaling, so both $ALG_1$ and $ALG_3$ lead to reasonably accurate mean flow predictions.

Last, we examine the behavior of the data-based models, i.e., $NN1_1$ and $NN2_1$. The results are shown in Fig. 14. We have

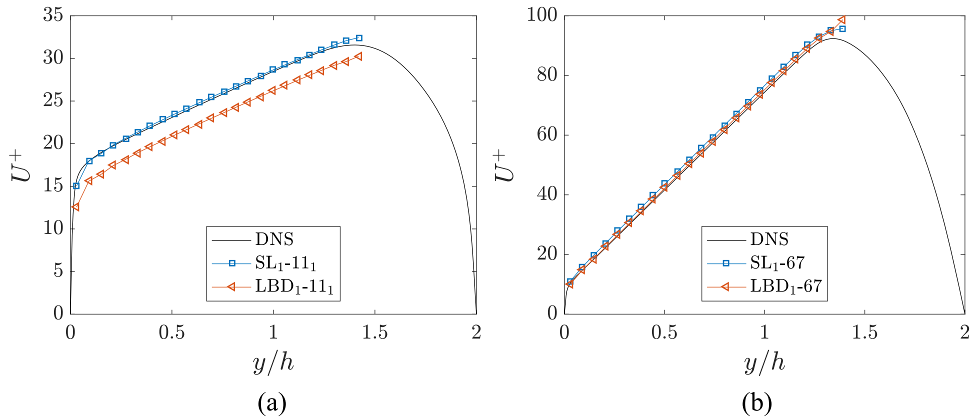


**FIG. 11**. Mean flows in (a) cases SL$_1$-11$_1$ and LBD$_1$-11$_1$ and their DNS counterpart and (b) cases SL$_1$-67 and LBD$_1$-67 and their DNS counterpart.

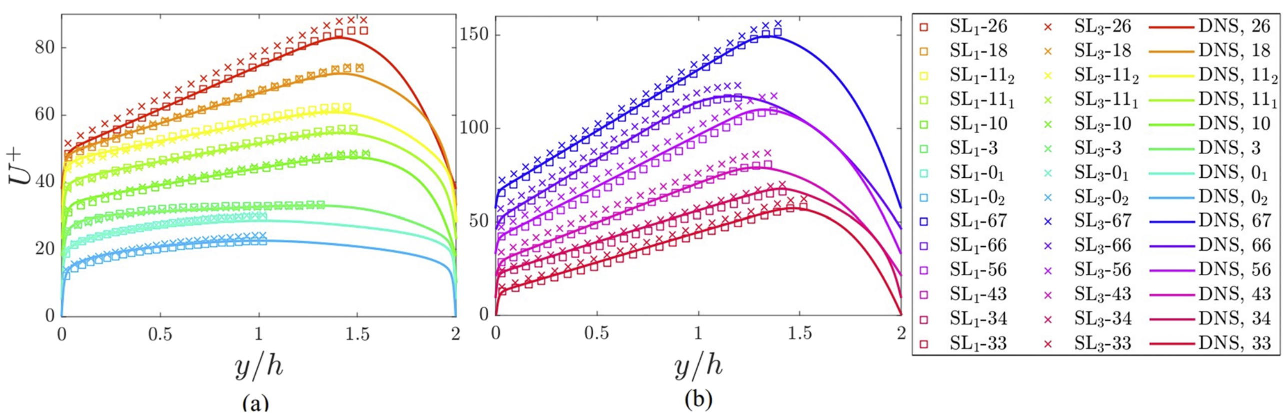


**FIG. 12**. Results of WMLESs that use the SL model and the corresponding DNSs.[23] Results of both SL$_1$ and SL$_3$ are shown. We use square symbols for SL$_1$ and cross symbols for SL$_3$. Solid lines are used for DNS results. (a) $0 \le Ro_\tau < 30$. (b) $30 < Ro_\tau \le 70$. The profiles are shifted vertically for clarification.

used the DNS data to train both NN1$_1$ and NN2$_1$. For these flow conditions, both NN1$_1$ and NN2$_1$ work well and yield very similar results. Comparing the SL model and the ALG model, we see that the data-based models seem to give more accurate mean flow predictions. This is probably not unexpected considering that the neural network is informed about the known physics and that there are closely 100 parameters, i.e., weights and biases, in the neural networks.

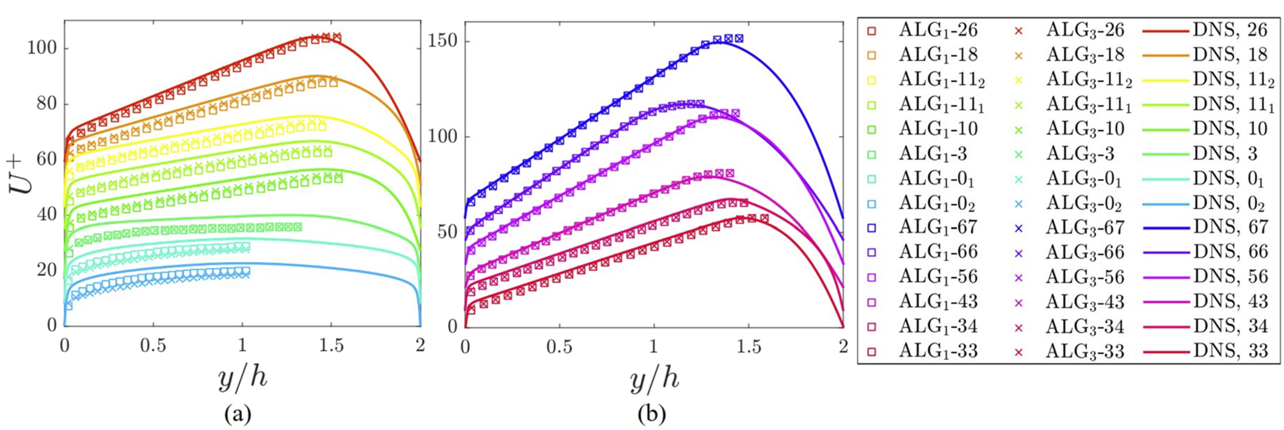


**FIG. 13**. Same as Fig. 12 but for ALG$_1$ and ALG$_3$.

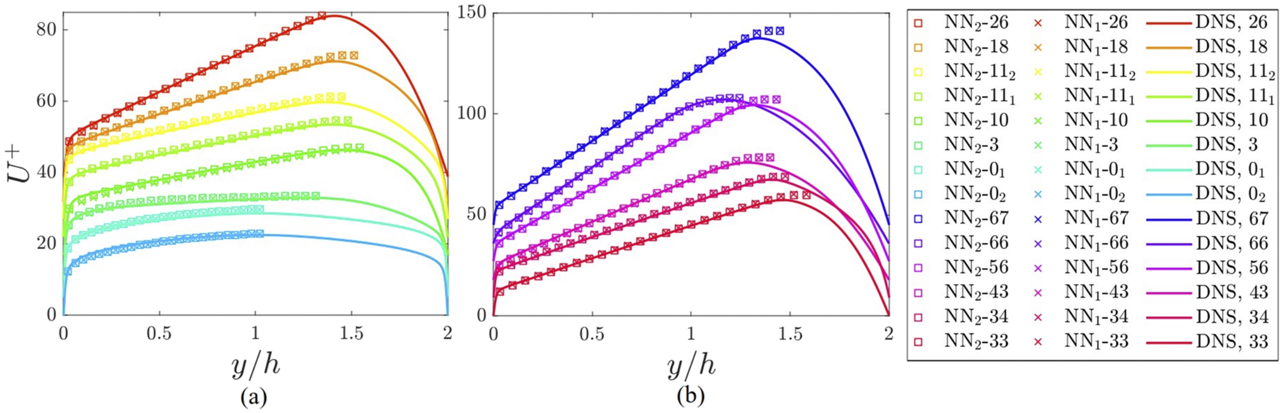


**FIG. 14**. Same as Fig. 12 but for NN1$_1$ and NN2$_1$.

### C. Turbulence statistics

LES solves the filtered Navier-Stokes equations and resolves only part of the turbulent kinetic energy. Figure 15 shows the premultiplied velocity spectra in a nonrotating channel and a rotating channel computed from the DNS counterparts of SL$_1$-0$_1$ and SL$_1$-33. The LES grid cuts off at $y^+ = 41.67$ and $\lambda_z^+ = 392.50$ in SL$_1$-0$_1$ and at $y^+ = 43.72$ and $\lambda_z^+ = 265.72$ in SL$_1$-33, and in our LES, we resolve only the scales above the grid cutoff. For SL$_1$-0$_1$, we resolve the outer peak, and at a given $y$, the energy in the subgrid scales is much smaller than that in the resolved scales. For SL$_1$-33, it is the opposite: there is more energy in the subgrid scales than in the resolved scales. The results are similar for other cases with spanwise rotation and are not shown for brevity. As we have already seen in Subsection IV B, although much of the turbulent kinetic energy is not resolved in our LESs, the LESs still give very accurate mean flow prediction. In this subsection, we will analyze terms in the momentum equation and the budget equation to find the reason.

We start our analysis by writing down the averaged LES momentum equation

$$0 = -\frac{1}{\rho}\frac{d\widetilde{P}}{dx} + \nu\frac{d^2\langle\widetilde{u}\rangle}{dy} - \frac{d\langle\widetilde{u}'\widetilde{v}'\rangle}{dy} + \frac{d\tau_{12}}{dy}, \tag{27}$$

where $\tau_{12}$ is the SGS stress (note that the negative sign is absorbed into the definition of $\tau$ here), the tilde $\widetilde{(\cdot)}$ denotes an LES filtering, $()'$ is the fluctuation of the bracketed quantity, and the chevron $\langle\cdot\rangle$ is the ensemble average of the bracketed quantity. Note that the turbulence eddy viscosity $\nu_T$ is dynamically computed and varies with time. Integrating Eq. (27) from the wall to a distance $y$, we obtain

$$\frac{\tau_w}{\rho} + \frac{1}{\rho}\frac{d\widetilde{P}}{dx}y = -\langle\widetilde{u}'\widetilde{v}'\rangle + \nu\frac{d\widetilde{U}}{dy} + \tau_{12}. \tag{28}$$

Normalizing Eq. (28) with $u_{\tau,p}^2$ leads to

$$1 - \frac{y}{L_y} = -\langle\widetilde{u}'\widetilde{v}'\rangle^+ + \tau_v^+ + \tau_T^+, \tag{29}$$

where $\tau_v^+ = \nu\frac{d\widetilde{U}}{dy}/u_{\tau,p}^2$ is the viscous stress and $\tau_T^+$ is the SGS flux. Figure 16 shows the various terms in Eq. (29) in SL$_1$-0$_2$ (nonrotating, plane channel) and SL$_1$-34 (spanwise rotating channel). The same typical WMLES grid is used for both cases. In the nonrotating case, the resolved turbulent flux accounts for most of the turbulent flux, whereas in the rotating case, the resolved flux is comparable to the subgrid flux. Nonetheless, the sum of the terms recovers the

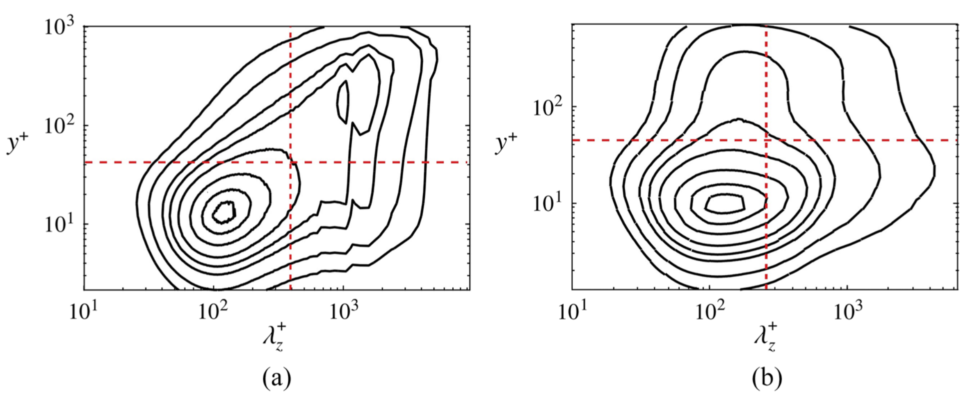


**FIG. 15**. The solid lines are contours of the premultiplied energy spectra $k_z E_{uu}$ of the streamwise velocity in the DNS counterparts of (a) SL$_1$-0$_1$ and (b) SL$_1$-33. Details of the DNS are presented in Ref. 23. The dashed lines correspond to the LES grid cutoffs, and they are at (a) $y^+ = 41.67$, $\lambda_z^+ = 392.50$; (b) $y^+ = 43.72$, $\lambda_z^+ = 265.72$.

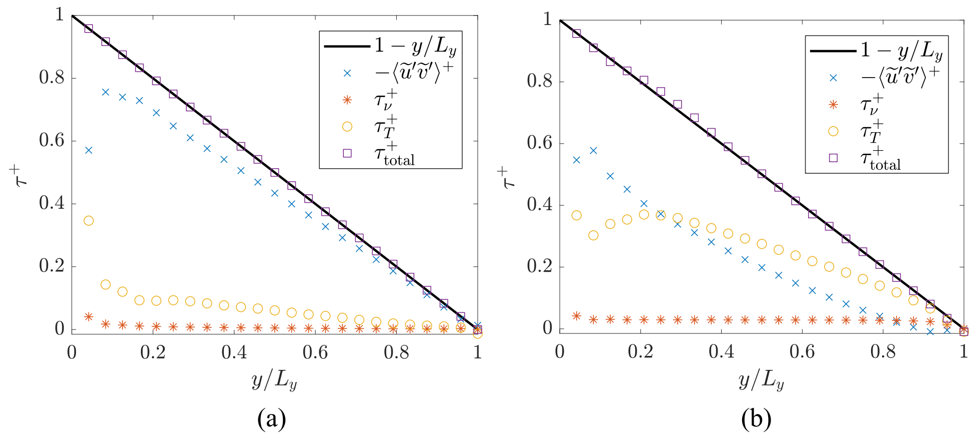


FIG. 16. The terms in Eq. (29) for (a) $SL_1$-$0_2$ and (b) $SL_1$-34. The total stress $\tau^+_{\rm total}$ is the sum of the viscous term, the resolved turbulent flux, and the subgrid flux.

expected linear scaling, $1 - y/L_y$. Figure 17 shows the velocity rms's. The velocity rms's in $SL_1$-$0_2$ are comparable to the DNS. On the other hand, the velocity rms's are underpredicted in $SL_1$-34 because the grid cutoffs are such that much of the energy is in the subgrid scales.

Last, we examine the budget equation of the resolved turbulent kinetic energy $k = \frac{1}{2}\langle\widetilde{u}_i'\widetilde{u}_i'\rangle$ in our fully developed half channels. The equation reads

$$0 = -\langle\widetilde{u}'\widetilde{v}'\rangle\frac{d\langle\widetilde{U}\rangle}{dy} - \frac{1}{2}\frac{d\langle\widetilde{u}_i'\widetilde{u}_i'\widetilde{v}'\rangle}{dy} - \frac{1}{\rho}\frac{d\langle\widetilde{p}'\widetilde{v}'\rangle}{dy} + \nu\frac{d^2k}{d^2y} - \nu\left\langle\frac{\partial\widetilde{u}_i'}{\partial x_j}\frac{\partial\widetilde{u}_i'}{\partial x_j}\right\rangle - \left\langle\widetilde{u}_i'\frac{\partial\tau_{ij}'}{\partial x_j}\right\rangle, \quad (30)$$

where $\tau_{ij}'$ is the fluctuation of the SGS stress tensor. The Coriolis force does not work and does not show up in the equation. Because LES does not resolve the viscous scales, many of the terms could not be compared to DNS in a way that makes apparent physical sense. Here, we only compare the production term, which is dominated by the large scales. Figure 18 shows the production term. Again, the term in $SL_1$-$0_2$ is comparable to DNS, and the term in $SL_1$-34 is underpredicted.

The analysis here has focused on one typical rotating case. The results are similar in other cases with system rotation and therefore are not shown here for brevity. In all, subgrid scale modeling is an important part of LES of flow with system rotation. As the focus of this work is LES wall modeling, detailed discussion of the subgrid scales and the modeling are left for future investigations.

### D. The ability to generalize

We conduct WMLESs at Reynolds numbers that are not yet possible for DNS, i.e., at $Re_{\tau,p} = 10^4$ and $10^5$. Details of the two high Reynolds number cases, i.e., $NN2_1$-71C and $NN2_1$-7C, are tabulated in Table IV. Applying a data-based model to flow at conditions that are outside the training dataset is usually a challenge for machine learning. In Sec. II D, we show that NN1, the neural network that is not informed about the flow physics, is not able to generalize and that NN2, the neural network that is physics-informed, is able to extrapolate to high Reynolds numbers. Here, we show that NN2 can truly extrapolate in the context of WMLES. The results are shown in Figs. 19(a) and 19(b), respectively. Although both flow conditions are outside the training dataset, the WMLES results follow the mean flow scalings closely.

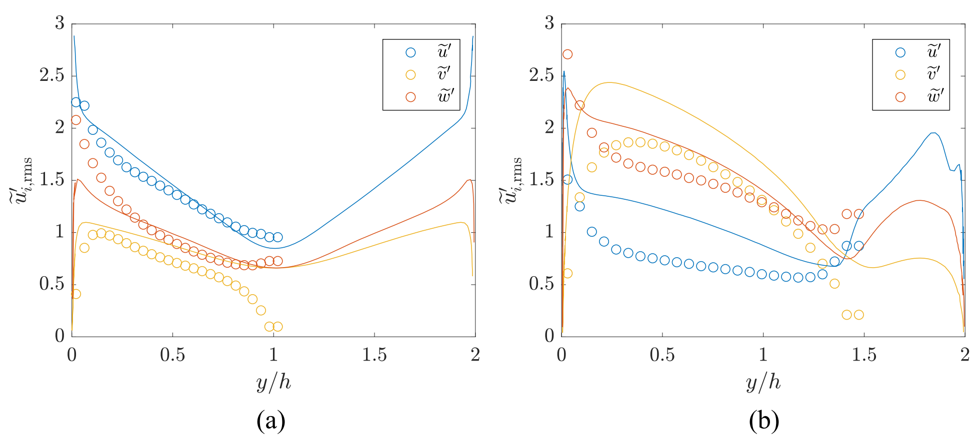


FIG. 17. Velocity rmss in (a) $SL_1$-$0_2$ and (b) $SL_1$-34. The symbols are the WMLES results, and the lines are the DNS results. We use color to distinguish different components.

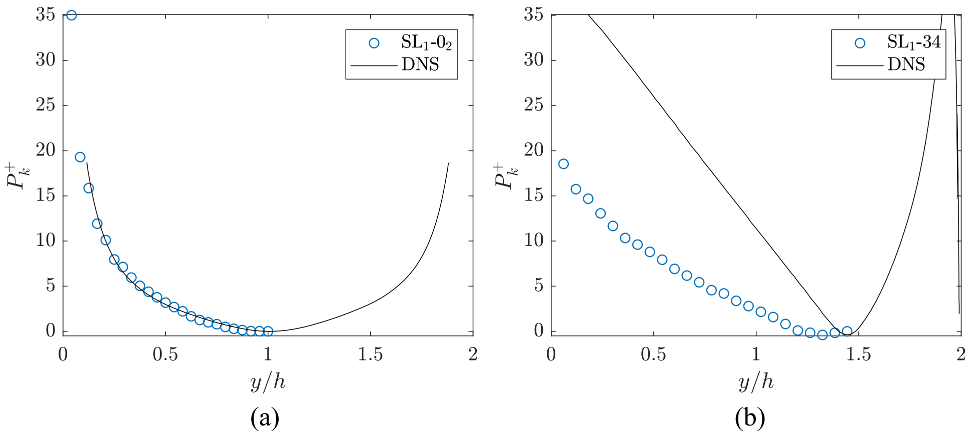


**FIG. 18**. Production term in the turbulent kinetic energy equation $P_k = -\langle\widetilde{u}'\widetilde{v}'\rangle \frac{\mathrm{d}\langle U\rangle}{\mathrm{d}y}$ in (a) $\mathrm{SL}_1$-$0_2$ and (b) $\mathrm{SL}_1$-34. The legends are the same as in Fig. 17.

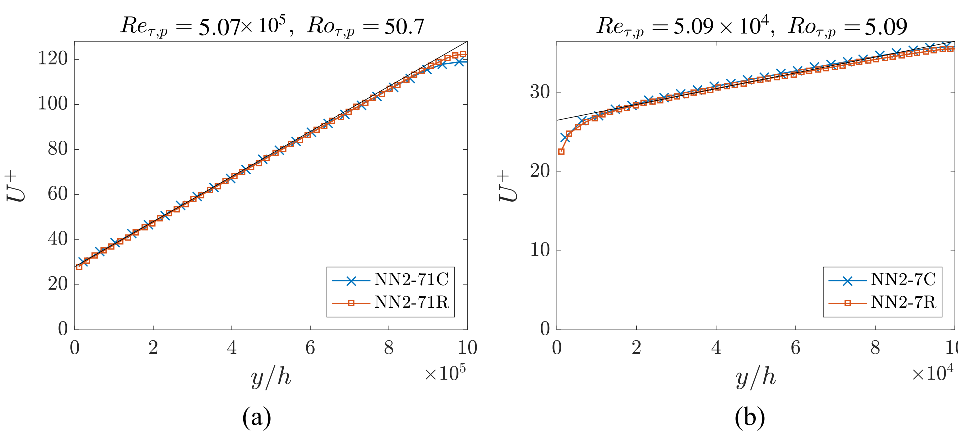


**FIG. 19**. (a) Mean velocity profiles in $\mathrm{NN2}_1$-71C and $\mathrm{NN2}_1$-71R. (b) Mean velocity profiles in $\mathrm{NN2}_1$-7C and $\mathrm{NN2}_1$-7R. The thin black line indicates the linear scaling. Details of the WMLESs are tabulated in Table IV.

In addition, we verify grid convergence by refining the grids of the two high Reynolds number cases, i.e., $\mathrm{NN2}_1$-71C and $\mathrm{NN2}_1$-7C, in all three Cartesian directions by a factor of 2. Because of the limited Reynolds numbers of the DNSs, the grid convergence study is only meaningful for flows at high Reynolds numbers. The cases in Table II are mostly at moderate Reynolds numbers. If one refines grids, the first off-wall grid would fall in the buffer layer or the viscous layer, which would not be meaningful for WMLES calculations. The cases that have refined grids are $\mathrm{NN2}_1$-71R and $\mathrm{NN2}_1$-71R, and details of the two cases are also tabulated in Table IV. The results are shown in Figs. 19(a) and 19(b), and we verify grid convergence.

## V. CONCLUSION

In this paper, we develop wall models for LES of spanwise rotating channel flow. The models accounts for system rotation yet preserves the ability to model flow in a nonrotating frame of reference.

Compared with flows in nonrotating frames of reference, e.g., boundary-layer flows and channel and pipe flows, flow subject to system rotation is less well understood, and conventional physics-based approaches do not have too much of an advantage compared to data-based approaches. As such, spanwise rotating channels are a good ground for testing and comparing a data-based approach and a physics-based approach, where data play a primary role and a secondary role, respectively.

When taking the physics-based approach, we model the effects of system rotation by modifying the mixing length. The developed model works well at all tested conditions. When taking the data-based approach, we train fully connected feed-forward neural networks using the available DNS data. Two networks are trained: one is informed about the flow physics and the other is not. Both networks work well for the flow conditions within the training dataset, but only the physics-informed network generalizes to conditions outside the training data. Compared with the physics-based model, the physics-informed machine learning model, i.e., the NN2 model, gives slightly more accurate mean flow predictions. The chronic problem of LLM, or rather linear-layer mismatch in this context, is not found in WMLES of the spanwise rotating channel at high rotational speeds even if one uses the unfiltered LES velocity at the first off-wall grid as the model input.

To summarize, we have developed a wall modeling capability for spanwise rotating channels, taking a physics-based approach and a data-based approach. Both approaches require human inputs: we have to make modeling choices when developing the physics based model and pick hyperparameters for the neural networks. A physics-based approach usually does not rely on data, and the developed model can be interpreted in a way that makes physical sense. The downside is that it requires an in-depth understanding of the flow phenomenon. On the other hand, developing a data-based approach is conceptually straight-forward if the data are available, and the developed model works very well for flow conditions within the training dataset. The disadvantages, however, are the need for data and a lack of interpretability (see Refs. 59 and 60 for recent developments on these two topics).

## ACKNOWLEDGMENTS

X.H. would like to thank Haosen Xu for fruitful discussions. The computations are conducted on Penn State ACI and XSEDE. X.Y. would like to thank Zhenhua Xia and David Williams for useful discussions.

## REFERENCES


[1] D. R. Chapman, "Computational aerodynamics development and outlook," AIAA J. **17**(12), 1293–1313 (1979).

[2] H. Choi and P. Moin, "Grid-point requirements for large eddy simulation: Chapman's estimates revisited," Phys. Fluids **24**(1), 011702 (2012).

[3] S. T. Bose and G. I. Park, "Wall-modeled large-eddy simulation for complex turbulent flows," Annu. Rev. Fluid Mech. **50**, 535–561 (2018).

[4] M. Inoue and D. I. Pullin, "Large-eddy simulation of the zero-pressure-gradient turbulent boundary layer up to $\mathrm{Re}_\theta = \mathcal{O}(10^{12})$," J. Fluid Mech. **686**, 507–533 (2011).

[5] R. J. Stevens, M. Wilczek, and C. Meneveau, "Large-eddy simulation study of the logarithmic law for second-and higher-order moments in turbulent wall-bounded flow," J. Fluid Mech. **757**, 888–907 (2014).

[6] X. I. A. Yang, J. Sadique, R. Mittal, and C. Meneveau, "Integral wall model for large eddy simulations of wall-bounded turbulent flows," Phys. Fluids **27**(2), 025112 (2015).

[7] M. G. Giometto, A. Christen, C. Meneveau, J. Fang, M. Krafczyk, and M. Parlange, "Spatial characteristics of roughness sublayer mean flow and turbulence over a realistic urban surface," Boundary-Layer Meteorol. **160**(3), 425–452 (2016).

[8] A. Lozano-Durán, M. Hack, and P. Moin, "Modeling boundary-layer transition in direct and large-eddy simulations using parabolized stability equations," Phys. Rev. Fluids **3**(2), 023901 (2018).

[9] G. I. Park and P. Moin, "An improved dynamic non-equilibrium wall-model for large eddy simulation," Phys. Fluids **26**(1), 015108 (2014).

[10] M. G. Giometto, A. Lozano-Duran, G. I. Park, and P. Moin, "Three-dimensional transient channel flow at moderate Reynolds numbers: Analysis and wall modeling," in *Center for Turbulence Research Annual Research Briefs* (Stanford, 2017), pp. 193–205.

[11] S. T. Bose and P. Moin, "A dynamic slip boundary condition for wall-modeled large-eddy simulation," Phys. Fluids **26**(1), 015104 (2014).

[12] J. Bodart and J. Larsson, "Wall-modeled large eddy simulation in complex geometries with application to high-lift devices," in *Center for Turbulence Research Annual Briefs* (Stanford, 2011), pp. 37–48.

[13] S. Kawai and J. Larsson, "Dynamic non-equilibrium wall-modeling for large eddy simulation at high Reynolds numbers," Phys. Fluids **25**(1), 015105 (2013).

[14] X. I. A. Yang, J. Urzay, S. Bose, and P. Moin, "Aerodynamic heating in wall-modeled large-eddy simulation of high-speed flows," AIAA J. **56**, 731–742 (2017).

[15] P. S. Iyer, G. I. Park, and M. R. Malik, "Wall-modeled large eddy simulation of transonic flow over an axisymmetric bump with shock-induced separation," in *23rd AIAA Computational Fluid Dynamics Conference* (AIAA, 2017), p. 3953.

[16] Y. Lv, X. I. A. Yang, G. I. Park, and M. Ihme, "Physics-based near-wall turbulence modeling in an enriched discontinuous Galerkin framework," in *Proceedings of the Summer Program* (Stanford, 2018), pp. 127–136.

[17] O. Lehmkuhl, G. I. Park, and P. Moin, "LES of flow over the NASA common research model with near-wall modeling," in *Proceedings of the Summer Program* (Stanford, 2016), pp. 335–341.

[18] J. P. Johnston, R. M. Halleent, and D. K. Lezius, "Effects of spanwise rotation on the structure of two-dimensional fully developed turbulent channel flow," J. Fluid Mech. **56**(3), 533–557 (1972).

[19] K. Nakabayashi and O. Kitoh, "Low Reynolds number fully developed two-dimensional turbulent channel flow with system rotation," J. Fluid Mech. **315**, 1–29 (1996).

[20] R. Kristoffersen and H. I. Andersson, "Direct simulations of low-Reynolds-number turbulent flow in a rotating channel," J. Fluid Mech. **256**, 163–197 (1993).

[21] O. Grundestam, S. Wallin, and A. V. Johansson, "Direct numerical simulations of rotating turbulent channel flow," J. Fluid Mech. **598**, 177–199 (2008).

[22] Z. Xia, Y. Shi, and S. Chen, "Direct numerical simulation of turbulent channel flow with spanwise rotation," J. Fluid Mech. **788**, 42–56 (2016).

[23] G. Brethouwer, "Statistics and structure of spanwise rotating turbulent channel flow at moderate Reynolds numbers," J. Fluid Mech. **828**, 424–458 (2017).

[24] S. Wallin, O. Grundestam, and A. V. Johansson, "Laminarization mechanisms and extreme-amplitude states in rapidly rotating plane channel flow," J. Fluid Mech. **730**, 193–219 (2013).

[25] G. Brethouwer, "Linear instabilities and recurring bursts of turbulence in rotating channel flow simulations," Phys. Rev. Fluids **1**(5), 054404 (2016).

[26] Y.-J. Dai, W.-X. Huang, and C.-X. Xu, "Effects of Taylor-Görtler vortices on turbulent flows in a spanwise-rotating channel," Phys. Fluids **28**(11), 115104 (2016).

[27] Y.-T. Yang and J.-Z. Wu, "Channel turbulence with spanwise rotation studied using helical wave decomposition," J. Fluid Mech. **692**, 137–152 (2012).

[28] P. E. Smirnov and F. R. Menter, "Sensitization of the SST turbulence model to rotation and curvature by applying the Spalart-Shur correction term," J. Turbomach. **131**(4), 041010 (2009).

[29] S. K. Arolla and P. A. Durbin, "Modeling rotation and curvature effects within scalar eddy viscosity model framework," Int. J. Heat Fluid Flow **39**, 78–89 (2013).

[30] U. Piomelli and J. Liu, "Large-eddy simulation of rotating channel flows using a localized dynamic model," Phys. Fluids **7**(4), 839–848 (1995).

[31] E. Lamballais, O. Métais, and M. Lesieur, "Spectral-dynamic model for large-eddy simulations of turbulent rotating channel flow," Theor. Comput. Fluid Dyn. **12**(3), 149–177 (1998).

[32] M. Silvis, F. X. Trias, M. Abkar, H. J. Bae, A. Lozano-Durán, and R. W. C. P. Verstappen, "Exploring nonlinear subgrid-scale models and new characteristic length scales for large-eddy simulation," in *Proceedings of the Summer Program* (Stanford, 2016), pp. 265–274.

[33] W. Rozema, H. J. Bae, P. Moin, and R. Verstappen, "Minimum-dissipation models for large-eddy simulation," Phys. Fluids **27**(8), 085107 (2015).

[34] N. A. Loppi, J. Bodart, and G. Dufour, "Wall-modeled large eddy simulation for rotating flows," in *Direct and Large-Eddy Simulation X* (Springer, 2018), pp. 263–269.

[35] X. I. A. Yang, Z.-H. Xia, J. Lee, Y. Lv, and J.-L. Yuan, "Mean flow scaling in a spanwise rotating channel," in *Center for Turbulence Research Annual Briefs* (Stanford, 2018), pp. 285–297.

[36] E. R. V. Driest, "On turbulent flow near a wall," J. Aeronaut. Sci. **23**(11), 1007–1011 (1956).

[37] K. Duraisamy, G. Iaccarino, and H. Xiao, "Turbulence modeling in the age of data," Annu. Rev. Fluid Mech. **51**, 357–377 (2019).

[38] J.-X. Wang, J.-L. Wu, and H. Xiao, "Physics-informed machine learning approach for reconstructing Reynolds stress modeling discrepancies based on DNS data," Phys. Rev. Fluids **2**(3), 034603 (2017).

[39] C. Cheng, W. Li, A. Lozano-Durán, and H. Liu, "Identity of attached eddies in turbulent channel flows with bidimensional empirical mode decomposition," J. Fluid Mech. **870**, 1037–1071 (2019).

[40] X. I. A. Yang, S. Zafar, J.-X. Wang, and H. Xiao, "Predictive large-eddy-simulation wall modeling via physics-informed neural networks," Phys. Rev. Fluids **4**(3), 034602 (2019).

[41] S. B. Pope, *Turbulent Flows* (Cambridge University Press, 2001).

[42] M. Hutson, "Has artificial intelligence become alchemy?," Science **360**, 478 (2018).

[43]J. Larsson, F. S. Lien, and E. Yee, "The artificial buffer layer and the effects of forcing in hybrid LES/RANS," Int. J. Heat Fluid Flow **28**(6), 1443–1459 (2007).
[44]N. V. Nikitin, F. Nicoud, B. Wasistho, K. D. Squires, and P. R. Spalart, "An approach to wall modeling in large-eddy simulations," Phys. Fluids **12**(7), 1629–1632 (2000).
[45]S. Kawai and J. Larsson, "Wall-modeling in large eddy simulation: Length scales, grid resolution, and accuracy," Phys. Fluids **24**(1), 015105 (2012).
[46]X. I. A. Yang, G. I. Park, and P. Moin, "Log-layer mismatch and modeling of the fluctuating wall stress in wall-modeled large-eddy simulations," Phys. Rev. Fluids **2**(10), 104601 (2017).
[47]E. Bou-Zeid, C. Meneveau, and M. B. Parlange, "Large-eddy simulation of neutral atmospheric boundary layer flow over heterogeneous surfaces: Blending height and effective surface roughness," Water Resour. Res. **40**(2), W02505 (2004).
[48]U. Piomelli, E. Balaras, H. Pasinato, K. D. Squires, and P. R. Spalart, "The inner-outer layer interface in large-eddy simulations with wall-layer models," Int. J. Heat Fluid Flow **24**(4), 538–550 (2003).
[49]P. Wu and J. Meyers, "A constraint for the subgrid-scale stresses in the logarithmic region of high Reynolds number turbulent boundary layers: A solution to the log-layer mismatch problem," Phys. Fluids **25**(1), 015104 (2013).
[50]S. Chen, Z. Xia, S. Pei, J. Wang, Y. Yang, Z. Xiao, and Y. Shi, "Reynolds-stress-constrained large-eddy simulation of wall-bounded turbulent flows," J. Fluid Mech. **703**, 1–28 (2012).
[51]J. Ling, R. Jones, and J. Templeton, "Machine learning strategies for systems with invariance properties," J. Comput. Phys. **318**, 22–35 (2016).
[52]C. Meneveau and J. Katz, "Scale-invariance and turbulence models for large-eddy simulation," Annu. Rev. Fluid Mech. **32**(1), 1–32 (2000).
[53]U. Piomelli and C. Scalo, "Subgrid-scale modelling in relaminarizing flows," Fluid Dyn. Res. **42**(4), 045510 (2010).
[54]E. Bou-Zeid, C. Meneveau, and M. Parlange, "A scale-dependent Lagrangian dynamic model for large eddy simulation of complex turbulent flows," Phys. Fluids **17**(2), 025105 (2005).
[55]X. I. A. Yang and M. Abkar, "A hierarchical random additive model for passive scalars in wall-bounded flows at high Reynolds numbers," J. Fluid Mech. **842**, 354–380 (2018).
[56]F. Porté-Agel, C. Meneveau, and M. B. Parlange, "A scale-dependent dynamic model for large-eddy simulation: Application to a neutral atmospheric boundary layer," J. Fluid Mech. **415**, 261–284 (2000).
[57]J. Larsson, S. Kawai, J. Bodart, and I. Bermejo-Moreno, "Large eddy simulation with modeled wall-stress: Recent progress and future directions," Mech. Eng. Rev. **3**(1), 15-00418 (2016).
[58]H. J. Bae, A. Lozano-Durán, S. T. Bose, and P. Moin, "Dynamic slip wall model for large-eddy simulation," J. Fluid Mech. **859**, 400–432 (2019).
[59]Y. Zhu, N. Zabaras, P.-S. Koutsourelakis, and P. Perdikaris, "Physics-constrained deep learning for high-dimensional surrogate modeling and uncertainty quantification without labeled data," J. Comput. Phys. **394**, 56–81 (2019).
[60]N. Geneva and N. Zabaras, "Modeling the dynamics of PDE systems with physics-constrained deep auto-regressive networks," preprint arXiv:1906.05747 (2019).